Enhanced Kinetics and Efficient Activation of Sulfur by Ultrathin MXene Coating S-CNTs Porous Sphere for High Stable and Fast Charging Lithium-Sulfur Batteries

ABSTRACT: Sulfur is an attractive material as commercial cathode because its theoretical capacity is five times higher than that of the current lithium ion batteries. The main challenges associated with Li-S batteries are terrible cycle stability, sluggish reaction kinetics and poor utilization especially at high current densities. Here, 3D S-CNT@MXene cages are proposed by a simple approach that resolve these critical problems. The 3D cages with interconnected conductive networks can improve sulfur utilization, decrease electrode resistance and enhance reaction kinetics. The covered layer of ultrathin MXene shell with high surface area with lots of terminal groups can prevent aggregation of MXene, increase chemical affinity, binding/interactions and catalytic effect with sulfur species to promote the adsorption of lithium polysulfides and nucleation of Li_2S. Moreover, the porous S-CNT sphere with sulfur nanoparticles on the surface of CNTs can facilitate electron transport, electrolyte infiltration and accommodation sulfur swelling. As a result, the 3D S-CNT@MXene cages cathode delivers a high discharge capacity of 1375.1 mAh g^{-1} at 0.1 C, high rate capacity (910.3 and 557.3 mAh g^{-1} at 1.0 and 8.0 C), and excellent cycling stability. Remarkably, the composite cathode shows almost no capacity fading (656.3 mAh g^{-1}) at a high current density of 4.0 C after 150 cycles, which shows the best cycling stability reported to date among all reported cathodes of Li-S batteries as per the knowledge.

KEYWORDS: S-CNT@MXene cages, S-CNT sphere, Lithium-Sulfur batteries, fast charging, cyclic stability

1. Introduction

The rapid development of consumer electronics and electric vehicles has put forward continues demand for high energy density storage systems and fast charging batteries.[1-3] Lithium-sulfur (Li-S) battery is regarded as one of the most promising next generation batteries because of the high energy density (2600 Wh kg^{-1}) and theoretical capacity (1675 mAh g^{-1}).[4-5] Meanwhile, the sulfur produced as a by-product of oil industry, is earth abundant, cheap and low toxicity.[5] However, sulfur cathode experiences several serious problems, especially at high current density, that hinder its practical applications as following: 1) sulfur ($\delta = 5 \times 10^{-30}$ S cm^{-1}) and its discharge product lithium sulfide (Li_2S, $\delta = 10^{-13}$ S cm^{-1}) are inherently insulating, resulting in low sulfur utilization and poor rate capacity; 2) the severe shuttle effect originated from the soluble of lithium polysulfides (LiPSs, Li_2S_n, $4 \leqslant n \leqslant 8$, formed during battery charging and discharging) in electrolytes causes rapid capacity decay and poor Coulombic efficiency;[6] 3) large volume change of active materials leads to the destroyed material architectures.[7] To solve the above challenges, several strategies have been explored including employment of composite sulfur host materials,[8] functionalization of separators,[9] and comprehensive design,[10] which enhance the reaction kinetics and promote utilization of active materials in Li-S batteries. Among all of these, the development of new sulfur-based composites is the most simple and effective method to improve the performance of Li-S batteries. Conductive carbon-based materials, such as mesoporous carbon,[11] carbon nanotubes (CNTs),[12] and graphene (GO),[13] can improve the conductivity and adapt the volume change of cathode. However, only physical adsorption is hardly to mitigate the shuttle effect due to the essentially nonpolar of carbon materials.[14] The polar metal oxides, such as TiO_2,[15] MnO_2,[16] have a strong chemical reaction towards to LiPSs, but inferior conductivity is difficult to meet the demand of fast reaction kinetics at high current density. The metal sulfides, like MoS_2,[17] and Co_9S_8,[18] have been used in Li-S batteries recently due to its good catalytic performance. But redundant side effects also limit its application.[19] In particular, developing novel materials of among these reported lead to the good cycle stability and rate capability only relatively to low current densities. It's hard to obtain good electrochemistry performance at a high current density for fast charging cathode due to weak reaction kinetics of sulfur-based composites.

A new class of polar two dimensional (2D) materials, MXenes ($M_{n+1}X_nT_x$; M = transition metal, X = C/N, n = 1/2/3, T = terminal groups, such as F/O/OH), were first reported by Gogotsi

in 2011.[20] MXenes have been widely investigated in energy storage materials due to its excellent conductivity and easily functionalized 2D surface.[21,22] Liang et al. firstly reported the application of Ti_2C MXene in Li-S batteries with improved electrochemical performance.[23] According to X-ray photoelectron spectroscopy (XPS) analysis, the terminal group OH is replaced by sulfide and then formed strong Ti-S bonds. However, 2D MXene nanosheets tend to restack like other 2D materials, which causes the limited surface area and utilization of Lewis acidic properties.[24,25] More recently, several composites including MXene/mesoporous carbon,[26] MXene/GO nanosheets,[27] and MXene/CNTs,[28,29] have been synthesized to overcome the disadvantage of MXene. Nazar et al. synthesized interwoven MXene nanosheets/carbon nanotube composites as Li-S cathode hosts.[29] The Ti-OH bonds on the surface of MXene provide plenty of nucleation sites of Li_2S due to its redox reaction with LiPSs. The addition of CNTs created an interwoven network that not only improved the overall conductivity but also prevented aggregation of MXene. However, CNT-MXene composites by direct mixing extremely easy to form bulk monolithic materials. The formation of layer by layer structure can effectively decrease the high surface area of individual MXene nanosheets, which can hinder electron transport and increase the ion diffusion path. Thus, it is still a challenge to explore a simple strategy to transform 2D MXene nanosheets and 1D CNTs into 3D architectures with high reaction kinetics of Li-S batteries at a high current density.

Herein, we report a facile and green method to assemble MXene coating sulfur and CNTs (S-CNT@MXene) micro cage that can be used as cathode for Li-S batteries with significantly improved capacity and cycle stability at a high current density. Firstly, sulfur was in-situ synthesized on the surface of CNTs to form S-CNT porous microspheres, and then ultrathin $Ti_3C_2T_x$ MXene nanosheets were used to wrap around the whole hollowed microspheres structure to form the 3D S-CNT@MXene cages. We report the development of the 3D S-CNT@MXene cages cathode with the following characteristics: (1) both CNT and MXene serve as good conducting network of the cages for fast electron transport to improve electrode resistance and enhance reaction kinetics; (2) sulfur distributed on the CNTs to improve the ion/electron accessibility and the sulfur utilization; (3) the outer ultrathin MXene coating layer effectively to avoid the shuttle effect of LiPSs, provide nucleation sites of Li_2S and prevent aggregation of MXene. (4) controlled empty spaces within the cages structure to accommodate

sulfur volume change and facilitate uniform Li_2S deposition. As a result, a significantly improved reaction kinetics at high current density for fast charging cathode was achieved. As expected, the S-CNT@MXene cathode delivered a high specific capacity of 1375.1 mAh g^{-1} at 0.1 C, remarkable rate performance especially at high current density (910.3, 557.3 mAh g^{-1} at 1.0 and 8.0 C, respectively). More importantly, the electrodes achieve a high capacity of 645.5 mAh g^{-1}, and a retention of 656.3 mAh g^{-1} after 150 cycles at a high discharging/charging rate of 4.0 C.

2. Experimental

2.1 Preparation of ultrathin MXene nanosheets

Typically, 1.0g lithium fluoride was dissolved into 20 mL hydrochloric acid (9.0 mol L^{-1}) to form clear solution by stirring for 10 minutes. Then 1.0 g Ti_3AlC_2 powders were added into above solution slowly, follow by string at 40 °C for 24 h. The suspension was centrifuged and washed with deionized (DI) water for several times until the pH > 6. After that, the wet precipitates were dispersed to 80 mL high purity water and sonicated for 2 h under N_2 atmosphere. The suspension was centrifuged for 1 h at 3500 rpm. The dark green supernatant was collected and continued to sonicate for another 6 h under N_2 atmosphere. Finally, the stable dispersion containing ultrathin MXene nanosheets of ~5 mg mL^{-1} was obtained.

2.2 Synthesis of S-CNT spheres

Firstly, the CNTs (diameter ~ 10 nm) were treated by nitric acid and sulfuric acid (volumetric ratio 1:2) overnight at 80 °C. The acid treated CNTs dispersed in DI water to form a stable suspension of 1 mg mL^{-1}. Then 0.04 mol L^{-1} Na_2S_4 solution was prepared by vigorously stirring sulfur and sodium sulfide at a molar ratio of 3:1 in DI water. The as-obtained 20 mL CNTs suspension added into 30 mL Na_2S_4 solution in an ice bath, and then 12 mL 0.4 mol L^{-1} acetic acid dropped into the above mixture at a very slow rate with continuous string. The sediment was washed by DI water for several times until pH neutral. After freeze dried, the S-CNT spheres were obtained.

2.3 Synthesis of S/CNT

The acid treated CNTs and the sulfur powder (produced by Na_2S_4 oxidation) at a weight ratio of 17:83 were mixed and grinded evenly.

2.4 Synthesis of S-CNT@MXene spheres

The as-prepared S-CNT spheres were dropped into MXene dispersion with string for 2 h, and then centrifuged for 5 minutes at 3500 rpm. Finally, the S-CNT@MXene spheres were obtained by freeze drying.

2.5 Characterizations

The morphology of samples were examined by using Hitachi S-4800 Scanning Electron Microscopy (SEM) and JEM-2100F Transmission Electron Microscopy (TEM). X-ray diffraction (XRD) patterns were collected by a D/max-2550 PC XRD (Rigaku, CuKα radiation). X-ray photoelectron spectroscopy (XPS) date was obtained using Escalab 250Xi. The BET surface area was measured by nitrogen adsorption/desorption on a JW-BK100C instrument. Thermal gravimetric analysis (TGA) were conducted in N_2 using Discovery TGA Q5000IR from 40 ℃ to 500 ℃ at a heating rate of 5 ℃ min^{-1}.

2.6 Visualized adsorption tests

The CNT@MXene spheres (CNT@MXene) were prepared by heating S-CNT@MXene spheres at 300 ℃ for 2 hours under N_2 to remove all the sulfur. Li_2S_6 soulution (10.0 mmol L^{-1}) was prepared by dissolving lithium sulfide and sulfur powder at a molar of 1:5 in 1:1 V/V DOL and DME. Then 10 mg CNT@MXene and CNTs were added into 3 ml of the above Li_2S_6 solution, respectively.

2.7 Assembly of Li_2S_6 symmetric cells

90 wt% active materials (CNT@MXene and acid treated CNT) and 10wt% PVDF were mixed in DMF then coated on carbon paper. The average weight loading of active materials is 1 mg cm^{-2}. The carbon paper was then cut into 1 × 1 cm squares and directly used as the electrodes. Afterwards, two identical electrodes were assembled into a 2032 cell with a PP

separator and 40 μL electrolyte of 0.1 M Li_2S_6 in 1:1 V/V DOL and DME. The black group used CNT@MXene as electrode and the electrolyte with no Li_2S_6 added. Cyclic voltammetry (CV) tests of symmetric cells were performed within a polarization of 1.0 V at scan rate of 3 mV s^{-1}.

2.8 Electrochemical tests

Typically, the active material (S-CNT@MXene, S-CNT, S/CNT), conductive agent (carbon black), and binder (PVDF) were mixed together to prepare the working electrode with a weight ratio of 8:1:1. The mass loading of active materials was 1.2 ± 0.1 mg cm^{-2}. Coin-type cells (CR2032) were fabricated using lithium metal as the anode and Celgard 2400 (Charlotte, NC, USA) as the separator. The electrolyte consisted of 1 M $LiPF_6$ dissolved in 1:1 V/V DOL and DME containing 2% $LiNO_3$. Galvanostatic discharge-charge tests were carried out on a LANDHE Measurement System (Landhe, China) with a cutoff voltage in the range of 2.8 V to 1.7 V(vs. Li/Li^+). Current densities and specific capacities were both calculated based on the sulfur loading on the working electrode (1C = 1675 mAh g^{-1}). CV measurements over the potential range of 1.7-2.8 V and electrochemical impedance spectroscopy (EIS) date in the frequency of 0.1 Hz to 100 kHz were conducted on an electrochemical workstation (Metrohm Autolab).

3. Results and discussion

Figure 1a illustrates the synthesis procedure of ultrathin MXene encapsulated hollowed microspheres composed with sulfur coated on the surface of CNTs to form three-dimension (3D) S-CNT@MXene cage structures. Firstly, multilayer MXene were prepared by etching to form a shape similar to accordion pulls open (Figure S1).[30] The ultrathin MXene nanosheets were obtained by extending ultrasonic. The surface of CNTs after acid-treated is negatively charged (Figure S2), coagulation occurred when adding acid. Na_2S_4 can be oxidized to sulfur on the surface of CNTs by adding acid to form porous spheres of mixed S-CNT. [31] Finally, ultrathin MXene was coated uniformly on the surface of S-CNT to form a 3D S-CNT@MXene cage by a simple mechanical stirring. In the synthesis process, the formation of

sulfur not only serves as the adhesives to support the 3D porous structure, but also acts as the active materials directly instead of additional melting step.[32] More importantly, this strategy can confine sulfur size on high-surface-area conducting CNTs, instead of bulk structure by the melt-diffusion method, which lead to high sulfur utilization and fast Lithium ion diffusion. Besides, the 3D structure of S-CNT@MXene not only improved the overall conductivity but also prevented aggregation of MXene, which improve the lithium ion diffusion path through the cathode.

Figure 1b is transmission electron microscopy (TEM) images of the obtained ultrathin MXene nanosheets. The $Ti_3C_2T_x$ nanosheets show ultrathin 2D layer structure with hundreds of nanometers. It should be noted that the MXene nanosheets were ultrathin with only one or two layers, which can be demonstrated via TEM images shown in Figure S3. The ultrathin 2D structure can improve the surface utilization of MXene. The inset high-resolution TEM (HRTEM) image (inset Figure 1b) indicate the high crystallinity of the ultrathin MXene flakes without obvious nanometer-scale defects or carbide amorphization, and an interplanar distance of ~0.23 nm can be assigned to the (103) planes of $Ti_3C_2T_x$.[33] The crystallinity of the prepared ultrathin MXene and the original Ti_3AlC_2 MAX phase crystals were investigated via X-ray diffraction (XRD), as displayed in Figure S4. The diffraction peak for the (104) planes of Ti_3AlC_2 located at 39° is absent and the main peak of (002) shifts from 9.5° to a much lower angle of 6.8°, indicating the successful preparation of the ultrathin MXene. There is no peaks of anatase or rutile type TiO_2 can be observed, demonstrating good stability of ultrathin MXene in the synthesis process. According to XRD, the interlayer space of MXene is 1.30 nm, slightly larger than other reports,[34] which also proved the successful synthesis of ultrathin MXene. The fourier transform infrared spectroscopy (FTIR) spectra of the ultrathin $Ti_3C_2T_x$ nanosheets (Figure S5) demonstrate two characteristic bonds at 3444 cm^{-1} and 1643 cm^{-1}, which are correspond to –OH and –C=O, respectively.[35]

The as synthesized S-CNT structure were uniform porous spheres (Figure 1c) with diameter of about 1.2 um based on field emission scanning electron microscopy (SEM). In the enlarged SEM image (Figure 1d), it is clear that all these CNTs with a large amount of sulfur materials are wrapped up after the reaction, forming an S-CNT porous spheres. Sulfur with nano-structured with diameter of 5-8 nm is preferentially attached to the surface of CNTs due to a

large number of defects and functional groups on the surface of CNTs after acid treated (Figure S6). These sulfur nanoparticles have close contact the surface of CNTs with diameter of about 10 nm, which can increase their electrical conductivity, enhance utilization of active materials and prevent sulfur aggregation during cycling with lithium ions. Besides, S-CNT porous spheres can effectively provide the volume expansion of sulfur during lithiation/delithiation process, which is beneficial for the stability of the structure.

The 3D S-CNT@MXene cage remained the spheres with similar size and morphology after coating with MXene nanosheets (Figure 1e). The 3D spherical structure of S-CNT@MXene avoids the restack of MXene and helps to make full use of active sites on the surface of MXene. In the enlarged SEM image (Figure 1f), the MXene wrapped on the surface of intertwined S-CNT closely, serving as highly conductive network to improve the overall conductance of the electrode film. HRTEM images in Figure 1g clear confirmed that the ultrathin MXene with only one layer or two layers tightly wrapped on the surface of S-CNT. As displayed in Figure 1h, an energy-dispersive X-ray spectroscopy (EDX) elemental mapping of S-CNT@MXene cage was detected, which clearly illuminates that C, Ti, S, O and F are uniformly distributed in the sphere region.

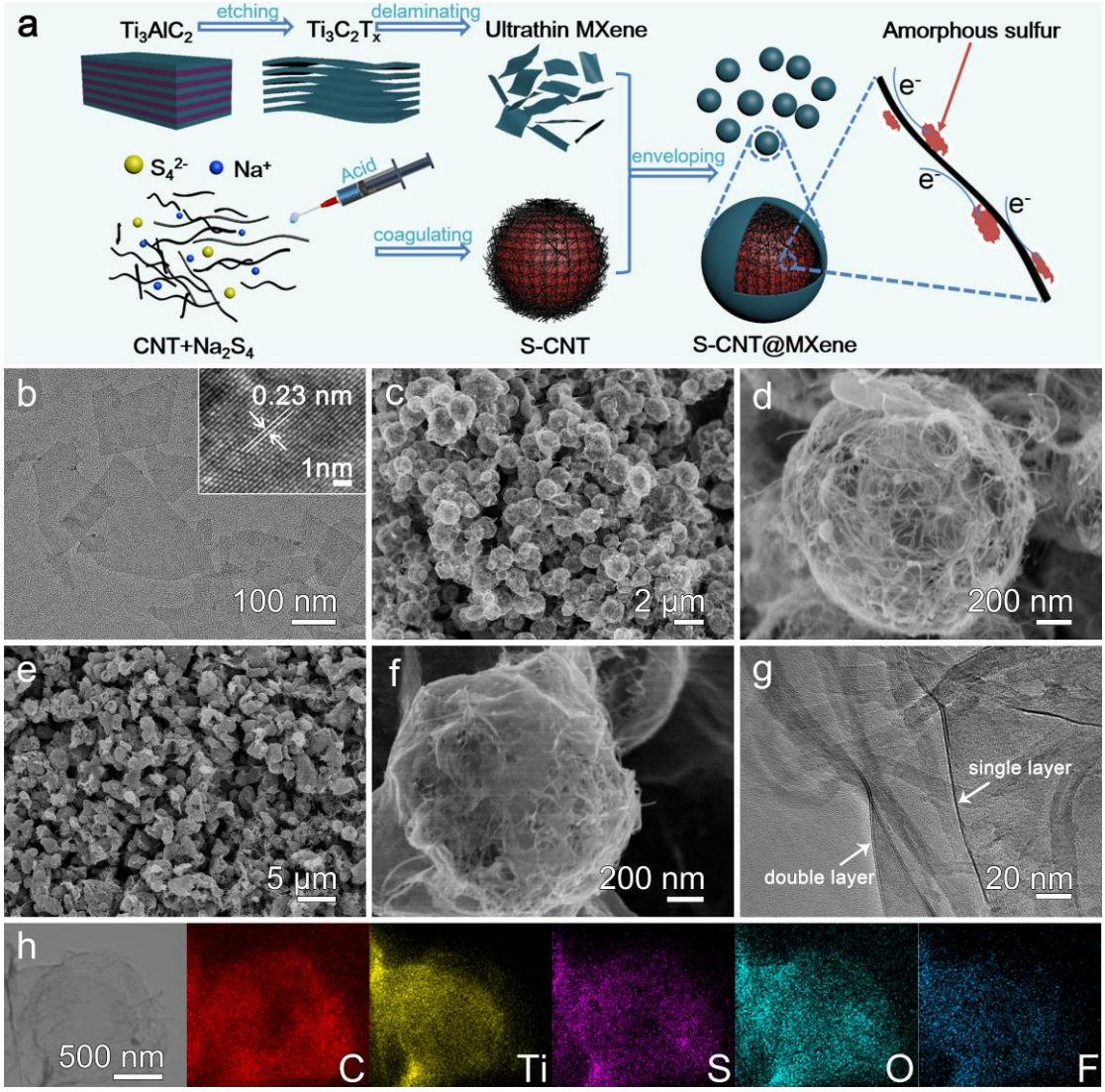

Figure 1 (a) Schematic illustration of the synthesis of 3D S-CNT@MXene cage spheres. (b) TEM image of ultrathin $Ti_3C_2T_x$ MXene; the inset show HRTEM of $Ti_3C_2T_x$ MXene. (c, d) SEM images of S-CNT spheres at different magnifications. (e, f) SEM images of 3D S-CNT@MXene cages at different magnifications. (g) HRTEM image of 3D S-CNT@MXene cages. (h) The EDX elemental mapping of 3D S-CNT@MXene cage, showing elements of C, Ti, S, O, and F, respectively.

To give further insight about the as-prepared 3D S-CNT@MXene composite, XRD and X-ray photoelectron spectroscopy (XPS) images are shown in Figure 2. Figure 2a shows the XRD pattern of S-CNT@MXene, S-CNT and elemental sulfur, respectively. Sulfur characteristic peaks appear in the XRD pattern of both S-CNT@MXene and S-CNT composites. But there is no obvious characteristic peak of MXene and CNTs because of the high sulfur content.[36] As

shown in Figure 2b, the thermogravimetric analysis (TGA) showed S-CNT@MXene cage to encapsulate sulfur materials with a high loading amount of 70 wt %. Compare to S-CNT, it can be calculated that the weight content of MXene is 15.7% in S-CNT@MXene, which can not only act as an attractive center for lithium sulfides but also catalyze the long-chain lithium polysulfide's conversion to insoluble short-chain lithium sulfides. To further confirm MXene encapsulation into the obtained S-CNT@MXene composite structure, XPS was conducted. As shown in Figure 2c, two strong peaks at 284.8 and 456.1 eV correspond to C1s and Ti2p, respectively.[37] Three weaker peaks at 531.4, 685.4 and 164.3 eV were identified, which can be assigned to O1s, F1s and S2p, respectively.[38] Furthermore, there is only 2.60 at% of element sulfur according to XPS elemental analysis (Table S1). In view of the surface specificity of XPS measurements, such significant difference between TGA and XPS elemental analysis results exactly verify almost all sulfur is wrapped inside by the 3D cages. The C1s can be resolved into three peaks at 282.2, 284.8 and 285.9 eV, corresponding to C-Ti, C-C and C-O bonds (Figure S7). C-O bonds are formed in the process of acid treatment of CNTs.[39] The high-resolution Ti2p spectrum shows several pairs of asymmetric peaks corresponding to the interactions between Ti and C as well as other terminal atoms (C-Ti-OH and C-Ti-O) in $Ti_3C_2T_x$ MXene (Figure 2d).[40] The existence of multiple terminal groups plays an important role in limiting shuttle effect and promoting the conversion of LiPSs. It has been proved that the -OH terminations are effective in entrapping long-chain sulfides such as Li_2S_4, Li_2S_6 and Li_2S_8, while the short-chain sulfides can be trapped by the -O groups,[41] followed by the Ti-S bond formation through a Lewis acid-base interaction.[29] Moreover, the specific surface area of CNT@MXene calculated is much higher than the pure $Ti_3C_2T_x$ MXene by BET method (Figure S8). The larger specific surface area is beneficial to the physical adsorption of LiPSs. Meanwhile, the implantation of MXene on the CNT sphere can significantly enhance its chemical adsorption with LiPSs owing to lots of terminal groups on the surface of MXene. To showcase this strong interaction between the 3D cage spheres and LiPSs, a visualized adsorption experiment of CNT@MXene in Li_2S_6 solution (10 mmol) was carried out (Figure 2e). The solution turned from dark yellow to transparent after 4 hours of adding the CNT@MXene, which indicates that the Li_2S_6 in the electrolyte is almost absorbed on the CNT@MXene. As for the solution added CNTs, the color is still yellow because of the weak adsorption by nonpolar CNTs. The UV/vis spectra was

further employed to illustrate the strong chemical interaction between CNT@MXene and LiPSs (Figure 2f). The solution with CNT@MXene shows the lowest absorption peak of lithium polysulfides, which proved that the 3D cages can adsorb LiPSs effectively and inhibit the shuttle effect.

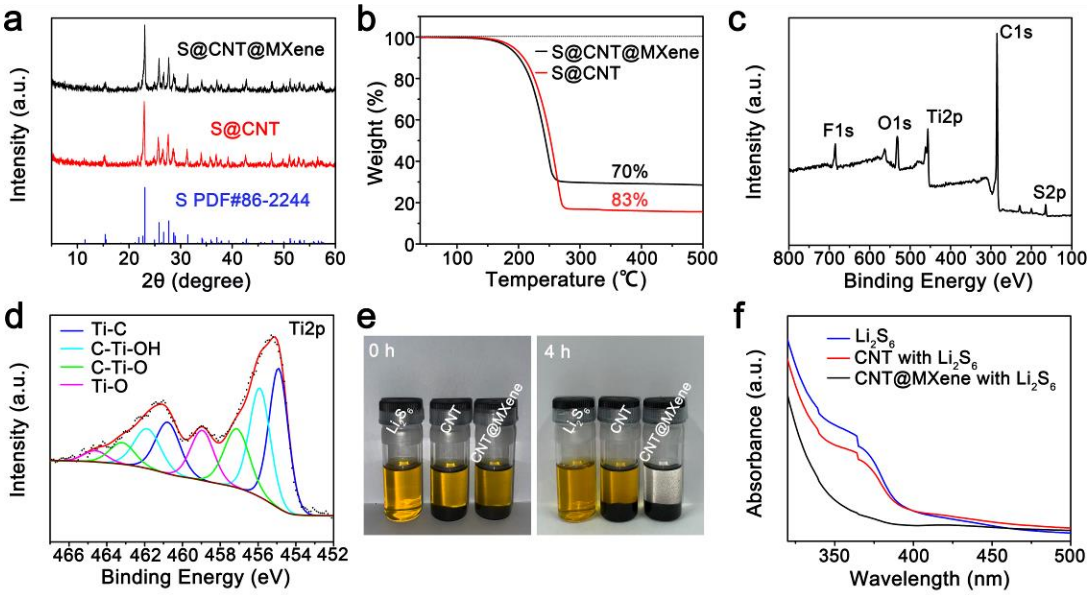

Figure 2. (a) XRD patterns of S-CNT@MXene composite, S-CNT composite and raw sulfur. (b) TG analysis curves of S-CNT@MXene composite and S-CNT composite. (c) XPS full-spectrum of S-CNT@MXene composite. (d) High-resolution XPS spectra of Ti2p in S-CNT@MXene composite. (e) Visual adsorption tests of CNT@MXene composite, CNT and Li_2S_6. (f) The UV/vis spectra of CNT@MXene composite, CNT and Li_2S_6.

To evaluate the electrochemical improvements of the Li-S cells using the S-CNT@MXene cathode, a series of electrochemical measurements were performed on the assembled 2032 coin cells. As shown in Figure 3a, the cyclic voltammetry (CV) curves of the S-CNT@MXene, S-CNT and S/CNT at a scan rate of 0.1 mV s^{-1}. Two reduction peaks and two oxidation peaks are obvious observed, which correspond to the lithiation process from S_8 to Li_2S_n ($4 \leq n \leq 8$; peak A) and final reduction to Li_2S_2 and Li_2S (peak B), the oxidation peaks are associated with reversed transformation of above process (peak C and D).[42] Although all of the three cathodes show similar CV curves, but the positions of the redox peaks and peak current densities are widely different, which indicates the different electrochemical reactivity.[19] Remarkably, two

cathodic peaks show distinct positive shift and higher peak current, indicating the enhanced transformation of S_8 to soluble Li_2S_n and further to insoluble Li_2S. This important improvements of reaction kinetics in electrochemical reaction can be attributed to the excellent conductivity of 3D S-CNT@MXene structure and catalytic activity of MXene, which promote the transfer of ions/electrons, and promote the nucleation of Li_2S on MXene with abundant active sites. Correspondingly, the anodic peak displays negative shifts, further demonstrating the structure 3D conductivity of 3D S-CNT@MXene facilitate the oxidation of Li_2S to S_8. However, the larger overvoltage and smaller peak current of S-CNT and S/CNT show the slow chemical reactivity and decrease utilization of sulfur.

To understand the importance of the promotion of S-CNT@MXene on lithium-ion diffusion more clearly, CV curves at different scanning rates were performed (Figure 3b, c and Figure S9a) and corresponding I - $v^{1/2}$ (I stands for current density and v stands for scanning rate) fitting lines at each redox current peaks are given in Figure 3d, e and Figure S9b. It shows that the peak currents of S-CNT@MXene have good linear relationship with the square root of scanning rates, indicating that the reaction is controlled by Li^+ diffusion. The diffusion coefficient of lithium ion (D_{Li^+}) can be calculated by the Randles-Sevcik equation,[43] $I = 2.686 \times 10^5 n^{1.5} A D_{Li^+} C v^{0.5}$. The slopes of $I - v^{1/2}$ of S-CNT@MXene cathode (4.07, 5.57, 8.69 for peaks A, B, C; Figure 3d) are much larger than that of S-CNT (3.30, 3.83, 5.75 for peaks A, B, C; Figure 3e) and S/CNT (3.20, 3.29, 5.55 for peaks A, B, C; Figure S9b), indicating that the S-CNT@MXene cathode has a much faster lithium ion transport. Meanwhile, as the scanning rate increases, the trend of the current of S-CNT@MXene increase is greater than those of the S-CNT and S/CNT. The S-CNT@MXene cathode can effectively strengthen the electron-transfer kinetics and provide unblocked Li^+ diffusion channels to speed up ionic/electronic transport, which can not only improve the utilization of sulfur but also ensure high-rate performance. Furthermore, Figure S10 shows the contact angle measurement to investigate the wettability of electrolyte on S-CNT@MXene cathode. The contact angle becomes almost 0° immediately when the electrolyte contacts the S-CNT@MXene cathode. Polar terminal groups on the surface of MXene facilitate better affinity with polar electrolyte, promoting the Li^+ transport.

We also tested the CV of symmetric cell with Li_2S_6 in electrolyte (Figure 3f) to further demonstrate the catalytic capability of MXene towards LiPSs redox reaction. CNT@MXene

presents enhanced redox current in contrast to CNT with a polarization of 1.0 V at a sweep rate of 3 mV s^{-1}, suggesting faster reaction kinetics and superior catalytic activity. Moreover, the redox peaks of CNT@MXene show much smaller polarization, indicating that is a smaller conversion barrier between the polysulfides in the 3D cages structure. These results verify the outstanding catalytic activity of CNT@MXene toward sulfur redox reactions due to a Lewis acid-base interaction between plenty of terminal groups and LiPSs.

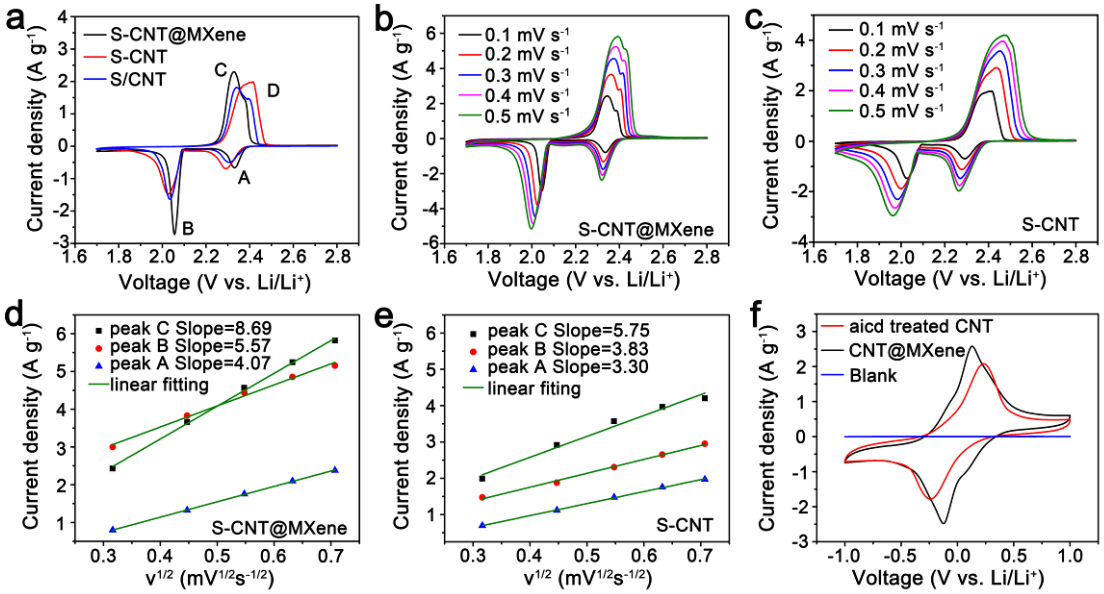

Figure 3. (a) CV curves of S-CNT@MXene, S-CNT and S/CNT cathodes in a potential range of 1.7-2.8 V at 0.1 mV s^{-1}. (b,c) The CV profiles at different scanning rates of S-CNT@MXene and S-CNT cathodes. (d,e) The corresponding I-$v^{1/2}$ slope curves of cells with S-CNT@MXene and S-CNT cathodes. (f) CV curves of CNT@MXene and CNT symmetric cells using 0.1 M Li_2S_6 electrolyte at 3 mV s^{-1}.

The structure design of 3D S-CNT@MXene cages provides remarkable performance of Li-S battery. Figure S11 shows the galvanostatic discharge-charge profiles of S-CNT@MXene, S-CNT and S/CNT electrodes under the current density of 0.1 C. The discharge plateaus around 2.35 and 2.1 V are attributed to reduction of sulfur to LiPSs and further reduction to Li_2S_2 and Li_2S, which is agreement with the CV curves based on the multi-step sulfur reduction mechanism. Obviously, the S-CNT@MXene cathode shows the smallest overpotential and highest discharge/charge capacity of 1375.1, 1283.1 mAh g^{-1}. As for S-CNT and S/CNT, the

discharge and charge capacities are only 1031.5, 977.1 mAh g^{-1} and 781.7, 732.6 mAh g^{-1}, respectively. The well uniformly dispersing of sulfur on conductive CNTs facilitated the utilization of active materials. Figure 4a showed the excellent rate performance, especially at high current densities. As shown, the S-CNT@MXene electrode exhibits capacity as high as 910.3 to 841.7, 745.5, 672.9 and 557.3 mAh g^{-1} at a charge-discharge rate of 1.0, 2.0, 4.0, 6.0, and 8.0 C, respectively. After cycling at the high current density of 8.0 C, the capacity could be recovered to 864.9 mAh g^{-1} when the current density decreases to 1.0 C, which corresponds to capacity retention of ~93% and demonstrates an excellent reversibility of the electrode after high current density. In addition, S-CNT and S/CNT experienced severe capacity degradation when the current density gradually increased. The capacity decreases by 51.9% of S-CNT when the current increases from 6.0 to 8.0 C and the capacity decreases by 42.4% of S/CNT when the C-rate from 2.0 to 4.0 C (Figure S12), indicating a sharp reduction upon sulfur utilization at high current densities. Compared with the S-CNT and S/CNT electrodes, the rate performance of the S-CNT@MXene electrodes are significantly higher, particularly at high current densities. Impressively, the improvement is more significant at high current density of 8.0 C, 3 times larger than that of S-CNT cathode and 5 times larger than that of S/CNT cathode. Such excellent rate performance at high current densities is extremely competitive compared with other previous work (Table S2).

Generally, high current density for lithiation and delithiation of sulfur electrodes is quite a huge challenge because of the slow conversion of polysulfide and poor conductivity of sulfur and Li_2S. The galvanostatic charge-discharge platform profiles of S-CNT@MXene cathode under different current densities are tested, as shown in Figure 4b. The charge-discharge platform shows smooth profiles with stable plateaus at high current density, even at 10.0 C, which suggest an efficient kinetic reaction process at high current density. The electrochemical performance at a high current density is highly correlated with the ion conductivity, the 3D high conductive well-connected networks with sulfur greatly improve the ion transmission.[44] The rapid reachability of ions and electrons ensures that the chemical reaction can proceed effectively. However, when current density increases to 6.0 C, the profiles of S-CNT cathode (Figure S13a) exhibit distinct distortion and big overpotential. This problem becomes more serious as the current density continues to increase and the discharge/charge platform profiles

disappear when current reaches 8.0 C, which indicates a large polarization and slow redox kinetics. As for S/CNT (Figure S13b), the problems of polarization and slow reaction kinetics are even worse. Figure 4c further shows that the potential gap (ΔV) between charge and discharge plateaus of S-CNT@MXene cathode is the smallest under different current densities (the ΔV of S/CNT and S-CNT exceed the measurable range when current density reaches 4.0 C and 8.0 C respectively). As a higher potential gap correspond to a more sluggish reduction of soluble LiPSs to insoluble Li_2S. The smallest potential gap indicates that the 3D cage structure transfers charge quickly and accelerates the redox reaction, which promote the transformation of polysulfide and nucleation of Li_2S, ensuring a higher sulfur utilization at a high current density. These results suggest that S-CNT@MXene cathode improves the kinetic reaction process for small nucleation overpotential, which has advantages in high-energy density and fast-charging capability.

The cycling performance was also investigated at high current densities. As displayed in Figure 4d, S-CNT@MXene cathode delivers a capacity of 645.5 mAh g^{-1} at the second cycle (the first cycle for activation materials at 0.1 C) and exhibits a reversible capacity of 656.3 mAh g^{-1} after 150 cycles at 4.0 C, which capacity retention is as high as ~100%. On average, S-CNT@MXene cathode electrode showed capacity retention of ~100%, which shows the best cycling stability reported to date among all reported S-based cathodes at a high current density as per the knowledge. S-CNT cathode also gives a specific capacity of 343.8 mAh g^{-1} after 150 cycles with 68% retention, while S/CNT leads to a performance even not exceeding 300 mAh g^{-1}. Furthermore, the long-cycle stability was also evaluated at a current density of 6.0 C for 700 cycles (Figure 4e). The S-CNT@MXene cathode delivers a maximum capacity of 627.0 mAh g^{-1} and retains a prominent capacity stability during 700 cycles with negligible capacity decay of 0.057% per cycle, which also illustrates the remarkable cycling stability of S-CNT@MXene at high current density. It is worth mentioning that during the long-term cycling, the average coulombic efficiency is higher than 98.2 %, demonstrating that the shuttling effect has been efficiently suppressed by the 3D cages structure assembled by ultrathin MXene and CNTs interwoven network. Besides, we also tested the CNT@MXene as cathodes under the same conditions, the results showed that CNT@MXene provided almost no capacity contribution (Figure S14). In sharp contrast, the capacity of S-CNT cathode decays quickly

from 452.1 to 121.6 mAh g^{-1} after 400 cycles and the S/CNT cathode delivers a very low capacity at high current density of 6.0 C.

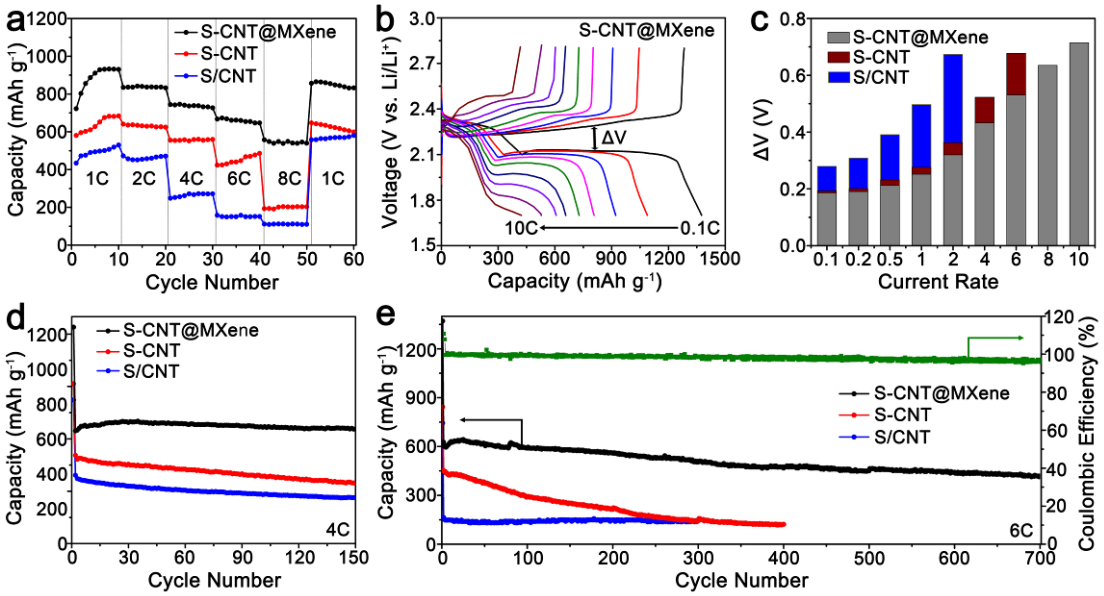

Figure 4. (a) Rate performances of S-CNT@MXene, S-CNT and S/CNT cathodes from 1.0C to 8.0C. (b) Galvanostatic discharge-charge profiles of S-CNT@MXene cathode at various current densities. (c) The potential gap (ΔV) between charge and discharge plateaus of S-CNT@MXene, S-CNT and S/CNT cathodes at different current densities. (d, e) Cycling performances of S-CNT@MXene, S-CNT and S/CNT cathodes at high current density of 4.0 C and 6.0 C.

For a deeper exploration of the excellent performance at high current densities for the kinetics effect of the S-CNT@MXene, electrochemical impedance spectra (EIS) measurements of the cells with S-CNT@MXene, S-CNT and S/CNT as cathodes were performed after high current density of 6.0 C. The EIS at fully charged were measured after 10th cycle, as shown in Figure 5a. The EIS consists of two semicircles at high frequencies and an inclined line in low frequency regions. The first high-frequency semicircles are attributed to the resistance of insulating layer of Li_2S and SEI on Li anode (Rg) after cycling.[45,46] This irreversible part of Li_2S caused the capacity loss, therefore, the stability of Rg represents the effectiveness of the redox reaction in cathode. The second semicircles at high frequency are involved with the charge transfer resistance (Rct) and the low-frequency line is related to the resistance originating from the ion

diffusion in the cathode (W). The intersection between the initial part of the first semicircle and the real axis represents the electrolyte resistance (Re).[47] It is obvious that the S-CNT@MXene cathode exhibits a smaller resistance both of Rg and Rct compared with the others, which could enable rapid electron transport and fast faradic reaction during Li^+ insertion/extraction processes. To further elucidate the stable electrochemical redox reaction of the 3D S-CNT@MXene cages and its strong adsorption to LiPSs, EIS changes were tested during long cycling (Figure 5c). The equivalent circuit was performed according to EIS (displayed in Figure 5d) and the results calculated from the simulation are summarized in Table S3. The Rct of S-CNT@MXene cell reduced to 9.85 Ω after 10th cycles, indicating the enhanced conductivity and improved the charge transferability during the previous cycling. More importantly, the Rct of S-CNT@MXene showed excellent cycling stability with no significant change after 400 cycles (10.91 Ω) at high current density. Moreover, the Rg of S-CNT@MXene cell stay stable from 10th cycle (6.74 Ω) to 400th cycle (5.12 Ω) at high current density, also implying the efficient redox reaction in the cell. As a result, the S-CNT@MXene provided significant advantages of rapid electron transport and fast faradaic reaction during the Li^+ insertion/extraction processes, which are favorable for increased capacity and longer cycling life at high current density. But as shown in Figure 5c, the Rct of S-CNT cell increased gradually as the continuous cycling (15.74, 17.86, 18.15, 27.69 Ω after 10th, 50th, 100th, 200th cycle, respectively), illustrating the conductivity obviously deteriorates during cycling. Meanwhile, the Li_2S formed during the discharge process cannot be effectively oxidized to lithium polysulfides resulting in the accumulation of insulation layer, leading to the Rg of the cell with S-CNT as cathode increases from 6.87 Ω (10th cycle) to 12.89 Ω (400th cycle). The Rct of the S/CNT cell have obviously increased due to the poor conductivity of sulfur cathode by the direct mixing of sulfur and CNTs (Figure S15).

Morphologies of the anode lithium metal of disassembled from S-CNT@MXene and S-CNT cells after cycles at 6.0 C were also examined with SEM, as shown in Figure 5e, f. Compared with fresh lithium metal before cycling (Figure S16), there is only a small amount of irregular materials attached on the surface of lithium metal from S-CNT@MXene cell after 50 cycles (Figure 5e). However, the surface of lithium from the S-CNT cell becomes rough and uneven (Figure 5f). From enlarged inset in Figure 5f, it is clearly that a thick layer of dead flake Li_2S

covered on the surface of lithium metal to prevent the rapid electron transport and fast faradaic reaction during cycle. Morphologies of the S-CNT@MXene electrode after 700 cycles at 6.0 C were also examined by SEM, as shown in Figure S17. It was found that the surface electrode of 3D S-CNT@MXene cages was well preserved without any apparent destruction, demonstrating S-CNT@MXene cages structural stability and MXene without self-restacking. It proved the structure of 3D S-CNT@MXene cages can buffer the volume change of sulfur during discharging and charging, which is also believed to the reason for improving cycle stability under high current density.

Figure 5g schematically illustrates the multiple advantages of S-CNT@MXene cage as cathode based on our design structure at high current density. Firstly, the porous S-CNT sphere with sulfur nanoparticles on the surface of CNTs forms a more open structures that maintain the structural stability of the composites. More importantly, S-CNT spheres inside S-CNT@MXene cage can greatly increase the electrical conductivity of sulfur and improve its utilization, offering a shortened diffusion pathway for rapid transport of ions and electrons, which is very important for enhanced electrochemical performance especially at high current density for fast discharge and charge. Secondly, the spherical structure prevents self-restacking of MXene to shorten the ion transport paths and diminish diffusion barrier of Li^+ to promote the sulfur redox kinetics. Moreover, the ultrathin MXene with large surface area provides abundant surface active sites to achieve strong interaction with LiPSs due to the high adsorption and catalyzes the conversion reaction of polysulfides, inhibit the shuttle effect effectively, and promote the conversion of LiPSs and nucleation of Li_2S through a Lewis acid-base interaction, that accelerating the electrochemical redox kinetics. Thirdly, the cage of S-CNT@MXene structure can effectively counteract the volume expansion of sulfur during discharging and charging, signifying improved cycle stability.

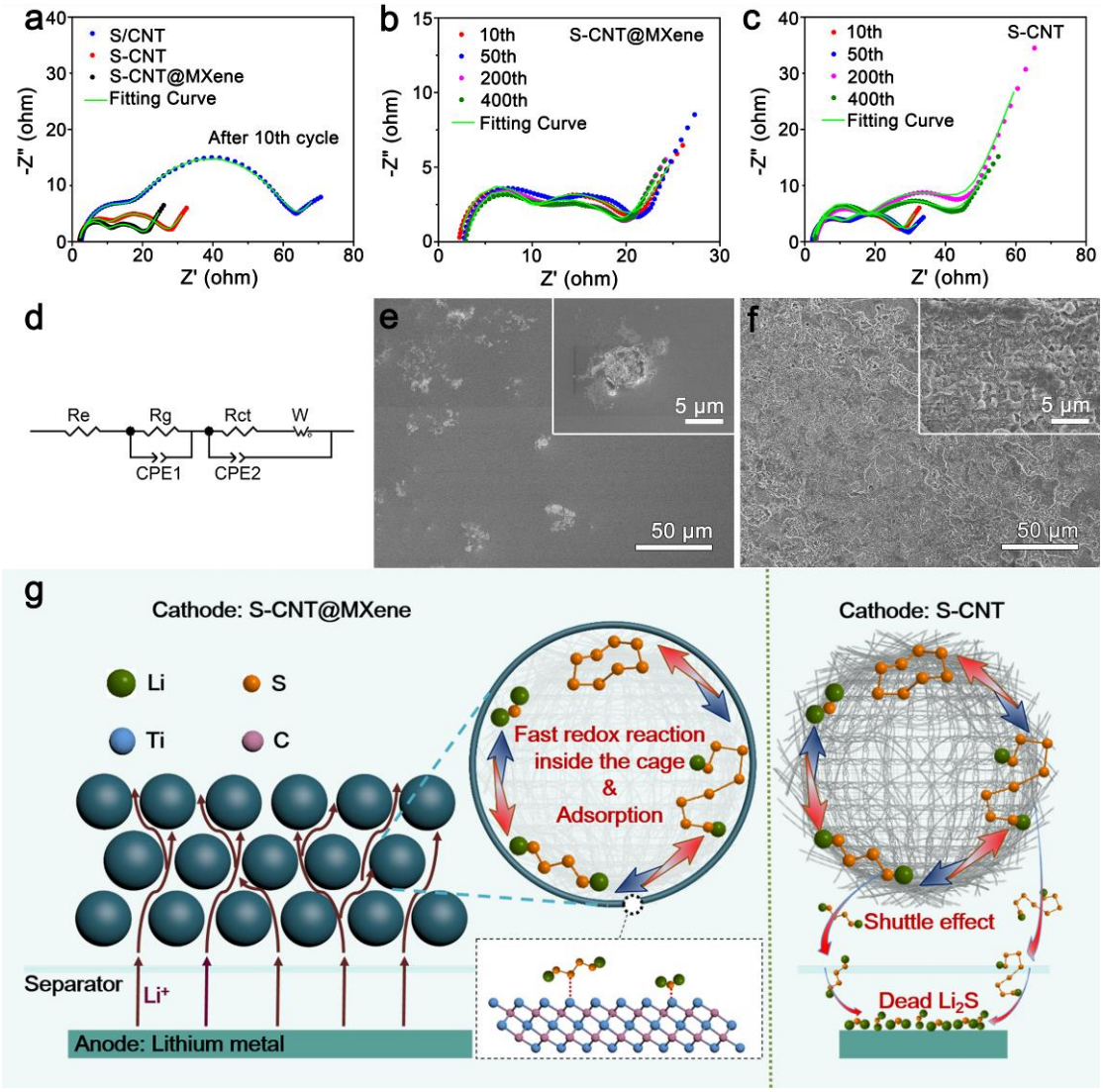

Figure 5. (a) EIS spectra of S-CNT@MXene, S-CNT and S/CNT cathodes after 10th cycle. (b, c) The EIS spectrum changes during cycling of the cells with S-CNT@MXene and S-CNT cathodes. (d) The equivalent circuit fitting for the Nyquist plot. (e, f) SEM images of surface for lithium metal disassembled from the cells with S-CNT@MXene and S-CNT as cathodes. (g) Schematic illustrating the electrochemical reaction of S-CNT@MXene (S-CNT) cathode in a working Li-S cell.

4. Conclusions

In summary, we successfully synthesized 3D S-CNT@MXene cages via a facile and green method (no additional energy is required to melt and fill sulfur). Within the cages, the CNTs cross through sulfur to form high-speed diffusion channels, which greatly enhanced the

conductivity of sulfur and insoluble Li_2S, facilitated the accessibility of electrons and ions and thus improved the utilization of sulfur and electrochemical redox kinetics. More importantly, the 3D structure of S-CNT@MXene avoided MXene restacking, improving the lithium ion diffusion path through the cathode. Meanwhile, the ultrathin MXene with large surface area provides abundant surface active sites to achieve strong interaction with LiPSs due to the high adsorption and catalyze the conversion reaction of LiPSs to Li_2S_2 and Li_2S, and effectively inhibited the shuttle effect. Finally, the cage of S-CNT@MXene structure can effectively counteract the volume expansion of sulfur during cycles. As a result, the S-CNT@MXene cathode exhibits a high initial capacity of 1365.1 mAh g^{-1} at 0.1 C, excellent rate performance (910.3, 557.3 mAh g^{-1} at 1.0 and 8.0 C, respectively), no capacity decay after 150 cycles at a high current density of 4.0 C. Furthermore, the electrode delivers an only 0.057% capacity decay per cycle over 700 cycles at a large current density of 6.0 C. This work demonstrated a rational design of high conductive cages can enhance the performance at high current densities of Li-S batteries, which is of great significance for application of high capacity and fast charge-discharge energy storage system.

ASSOCIATED CONTENT

Supporting Information

The Supporting Information is available free of charge at https://pubs.acs.org/

Notes

The authors declare no competing financial interest.

ACKNOWLEDGMENTS

We acknowledge the financial support from the National Natural Science Foundation of China (Grant No. 11974074 and 11804048), the Program Innovative Research Team in University (IRT_16R13), the Fundamental Research Funds for the Central Universities, the Science and Technology Commission of Shanghai Municipality (18ZR1402000), and the International Joint Laboratory for Advanced fiber and Low-dimension Materials (18520750400).

REFERENCES

1. Liu, H.; Zhu, Z.; Yan, Q.; Yu, S.; He, X.; Chen, Y.; Zhang, R.; Ma, L.; Liu, T.; Li, M.; Lin, R.; Chen, Y.; Li, Y.; Xing, X.; Choi, Y.; Gao, L.; Cho, H. S.-y.; An, K.; Feng, J.; Kostecki, R.; Amine, K.; Wu, T.; Lu, J.; Xin, H. L.; Ong, S. P.; Liu, P., A disordered rock salt anode for fast-charging lithium-ion batteries. *Nature* **2020,** *585* (7823), 63-67.
2. Cai, W.; Yao, Y.-X.; Zhu, G.-L.; Yan, C.; Jiang, L.-L.; He, C.; Huang, J.-Q.; Zhang, Q., A review on energy chemistry of fast-charging anodes. *Chemical Society Reviews* **2020,** *49* (12), 3806-3833.
3. Zhang, J.; Yang, C.-P.; Yin, Y.-X.; Wan, L.-J.; Guo, Y.-G., Sulfur Encapsulated in Graphitic Carbon Nanocages for High-Rate and Long-Cycle Lithium-Sulfur Batteries. *Adv. Mater.* **2016,** *28* (43), 9539-9544.
4. Manthiram, A.; Fu, Y. Z.; Su, Y. S., Challenges and Prospects of Lithium-Sulfur Batteries. *Accounts Chem. Res.* **2013,** *46* (5), 1125-1134.
5. Zhang, Z.; Kong, L.-L.; Liu, S.; Li, G.-R.; Gao, X.-P., A High-Efficiency Sulfur/Carbon Composite Based on 3D Graphene Nanosheet@Carbon Nanotube Matrix as Cathode for Lithium-Sulfur Battery. *Adv. Energy Mater.* **2017,** *7* (11) , 1602543.
6. Wang, Y. Z.; Huang, X. X.; Zhang, S. Q.; Hou, Y. L., Sulfur Hosts against the Shuttle Effect. *Small Methods* **2018,** *2* (6), 1700345.
7. Zhang, J.; Li, Z.; Chen, Y.; Gao, S.; Lou, X. W., Nickel-Iron Layered Double Hydroxide Hollow Polyhedrons as a Superior Sulfur Host for Lithium-Sulfur Batteries. *Angew. Chem.-Int. Edit.* **2018,** *57* (34), 10944-10948.
8. Li, Z.; Wu, H. B.; Lou, X. W., Rational designs and engineering of hollow micro-/nanostructures as sulfur hosts for advanced lithium-sulfur batteries. *Energy Environ. Sci.* **2016,** *9* (10), 3061-3070.
9. Li, Z.; Zhou, C.; Hua, J.; Hong, X.; Sun, C.; Li, H.-W.; Xu, X.; Mai, L., Engineering Oxygen Vacancies in a Polysulfide-Blocking Layer with Enhanced Catalytic Ability. *Adv. Mater.* **2020,** *32* (10) , 1907444.
10. Huang, X.; Tang, J.; Luo, B.; Knibbe, R.; Lin, T.; Hu, H.; Rana, M.; Hu, Y.; Zhu, X.; Gu, Q.; Wang, D.; Wang, L., Sandwich-Like Ultrathin TiS_2 Nanosheets Confined within N, S Codoped Porous Carbon as an Effective Polysulfide Promoter in Lithium-Sulfur Batteries. *Adv. Energy Mater.* **2019,** *9* (32), 1901872.
11. Hernandez-Rentero, C.; Cordoba, R.; Moreno, N.; Caballero, A.; Morales, J.; Olivares-Marin, M.; Gomez-Serrano, V., Low-cost disordered carbons for Li/S batteries: A high-performance carbon with dual porosity derived from cherry pits. *Nano Research* **2018,** *11* (1), 89-100.
12. Zheng, M.; Chi, Y.; Hu, Q.; Tang, H.; Jiang, X.; Zhang, L.; Zhang, S.; Pang, H.; Xu, Q., Carbon nanotube-based materials for lithium-sulfur batteries. *Journal Of Materials Chemistry A* **2019,** *7* (29), 17204-17241.
13. Li, H.; Tao, Y.; Zhang, C.; Liu, D.; Luo, J.; Fan, W.; Xu, Y.; Li, Y.; You, C.; Pan, Z.-Z.; Ye, M.; Chen, Z.; Dong, Z.; Wang, D.-W.; Kang, F.; Lu, J.; Yang, Q.-H., Dense Graphene Monolith for High Volumetric Energy Density Li-S Batteries. *Adv. Energy Mater.* **2018,** *8* (18), 1703438.
14. Zhang, L. L.; Wang, Y. J.; Niu, Z. Q.; Chen, J., Advanced nanostructured carbon-based materials for rechargeable lithium-sulfur batteries. *Carbon* **2019,** *141*, 400-416.
15. Salhabi, E. H. M.; Zhao, J.; Wang, J.; Yang, M.; Wang, B.; Wang, D., Hollow Multi-Shelled Structural TiO_{2-x} with Multiple Spatial Confinement for Long-Life Lithium-Sulfur Batteries. *Angew. Chem.-Int. Edit.* **2019,** *58* (27), 9078-9082.
16. Chen, M.; Lu, Q.; Jiang, S.; Huang, C.; Wang, X.; Wu, B.; Xiang, K.; Wu, Y., MnO_2 nanosheets grown on the internal/external surface of N-doped hollow porous carbon nanospheres as the sulfur host of advanced lithium-sulfur batteries. *Chemical Engineering Journal* **2018,** *335*, 831-842.

17. He, J.; Hartmann, G.; Lee, M.; Hwang, G. S.; Chen, Y.; Manthiram, A., Freestanding 1T MoS_2/graphene heterostructures as a highly efficient electrocatalyst for lithium polysulfides in Li-S batteries. *Energy Environ. Sci.* **2019,** *12* (1), 344-350.

18. Li, Z.; Xiao, Z.; Li, P.; Meng, X.; Wang, R., Enhanced Chemisorption and Catalytic Effects toward Polysulfides by Modulating Hollow Nanoarchitectures for Long-Life Lithium-Sulfur Batteries. *Small* **2020,** *16* (4), 1906114.

19. Wang, R.; Luo, C.; Wang, T.; Zhou, G.; Deng, Y.; He, Y.; Zhang, Q.; Kang, F.; Lv, W.; Yang, Q.-H., Bidirectional Catalysts for Liquid-Solid Redox Conversion in Lithium-Sulfur Batteries. *Adv. Mater.* **2020,** *32* (32), 2000315.

20. Naguib, M.; Kurtoglu, M.; Presser, V.; Lu, J.; Niu, J.; Heon, M.; Hultman, L.; Gogotsi, Y.; Barsoum, M. W., Two-Dimensional Nanocrystals Produced by Exfoliation of Ti_3AlC_2. *Adv. Mater.* **2011,** *23* (37), 4248-4253.

21. Xia, Y.; Mathis, T. S.; Zhao, M. Q.; Anasori, B.; Dang, A.; Zhou, Z. H.; Cho, H.; Gogotsi, Y.; Yang, S., Thickness - independent capacitance of vertically aligned liquid-crystalline MXenes. *Nature* **2018,** *557* (7705), 409-412.

22. Pang, J.; Mendes, R. G.; Bachmatiuk, A.; Zhao, L.; Ta, H. Q.; Gemming, T.; Liu, H.; Liu, Z.; Rummeli, M. H., Applications of 2D MXenes in energy conversion and storage systems. *Chemical Society Reviews* **2019,** *48* (1), 72-133.

23. Liang, X.; Garsuch, A.; Nazar, L. F., Sulfur Cathodes Based on Conductive MXene Nanosheets for High-Performance Lithium-Sulfur Batteries. *Angew. Chem.-Int. Edit.* **2015,** *54* (13), 3907-3911.

24. Lukatskaya, M. R.; Kota, S.; Lin, Z.; Zhao, M.-Q.; Shpigel, N.; Levi, M. D.; Halim, J.; Taberna, P.-L.; Barsoum, M.; Simon, P.; Gogotsi, Y., Ultra-high-rate pseudocapacitive energy storage in two-dimensional transition metal carbides. *Nat. Energy* **2017,** *2* (8), 17105.

25. Zhao, M.-Q.; Xie, X.; Ren, C. E.; Makaryan, T.; Anasori, B.; Wang, G.; Gogotsi, Y., Hollow MXene Spheres and 3D Macroporous MXene Frameworks for Na-Ion Storage. *Adv. Mater.* **2017,** *29* (37), 1702410.

26. Bao, W.; Su, D.; Zhang, W.; Guo, X.; Wang, G., 3D Metal Carbide@Mesoporous Carbon Hybrid Architecture as a New Polysulfide Reservoir for Lithium-Sulfur Batteries. *Adv. Funct. Mater.* **2016,** *26* (47), 8746-8756.

27. Liu, P.; Qu, L.; Tian, X.; Yi, Y.; Xia, J.; Wang, T.; Nan, J.; Yang, P.; Wang, T.; Fang, B.; Li, M.; Yang, B., $Ti_3C_2T_x$/Graphene Oxide Free-Standing Membranes as Modified Separators for Lithium-Sulfur Batteries with Enhanced Rate Performance. *Acs Applied Energy Materials* **2020,** *3* (3), 2708-2718.

28. Wang, J.; Zhang, Z.; Yan, X.; Zhang, S.; Wu, Z.; Zhuang, Z.; Han, W.-Q., Rational Design of Porous N-Ti_3C_2 MXene@CNT Microspheres for High Cycling Stability in Li-S Battery. *Nano-Micro Letters* **2020,** *12* (1), 4.

29. Liang, X.; Rangom, Y.; Kwok, C. Y.; Pang, Q.; Nazar, L. F., Interwoven MXene Nanosheet/Carbon-Nanotube Composites as Li-S Cathode Hosts. *Adv. Mater.* **2017,** *29* (3), 1603040.

30. Zuo, D. C.; Song, S. C.; An, C. S.; Tang, L. B.; He, Z. J.; Zheng, J. C., Synthesis of sandwich-like structured Sn/SnO_x@MXene composite through in-situ growth for highly reversible lithium storage. *Nano Energy* **2019,** *62*, 401-409.

31. Jiao, L.; Zhang, C.; Geng, C.; Wu, S.; Li, H.; Lv, W.; Tao, Y.; Chen, Z.; Zhou, G.; Li, J.; Ling, G.; Wan, Y.; Yang, Q.-H., Capture and Catalytic Conversion of Polysulfides by In Situ Built TiO_2-MXene Heterostructures for Lithium-Sulfur Batteries. *Adv. Energy Mater.* **2019,** *9* (19), 1900219.

32. Xing, Z.; Li, G.; Sy, S.; Chen, Z., Recessed deposition of TiN into N-doped carbon as a cathode host

for superior Li-S batteries performance. *Nano Energy* **2018,** *54*, 1-9.

33. Zheng, R.; Shu, C.; Hou, Z.; Hu, A.; Hei, P.; Yang, T.; Li, J.; Liang, R.; Long, J., In Situ Fabricating Oxygen Vacancy-Rich TiO_2 Nanoparticles via Utilizing Thermodynamically Metastable Ti Atoms on Ti(3)C(2)Tx MXene Nanosheet Surface To Boost Electrocatalytic Activity for High-Performance Li-O-2 Batteries. *ACS Appl. Mater. Interfaces* **2019,** *11* (50), 46696-46704.

34. Xiao, Z.; Li, Z.; Li, P.; Meng, X.; Wang, R., Ultrafine Ti_3C_2 MXene Nanodots-Interspersed Nanosheet for High-Energy-Density Lithium-Sulfur Batteries. *ACS Nano* **2019,** *13* (3), 3608-3617.

35. Shen, J.; Liu, G.; Ji, Y.; Liu, Q.; Cheng, L.; Guan, K.; Zhang, M.; Liu, G.; Xiong, J.; Yang, J.; Jin, W., 2D MXene Nanofilms with Tunable Gas Transport Channels. *Adv. Funct. Mater.* **2018,** *28* (31), 1801511.

36. Zhang, H.; Zou, M.; Zhao, W.; Wang, Y.; Chen, Y.; Wu, Y.; Dai, L.; Cao, A., Highly Dispersed Catalytic Co_3S_4 among a Hierarchical Carbon Nanostructure for High-Rate and Long-Life Lithium-Sulfur Batteries. *ACS Nano* **2019,** *13* (4), 3982-3991.

37. Lee, D. K.; Chae, Y.; Yun, H.; Ahn, C. W.; Lee, J. W., CO_2-Oxidized $Ti_3C_2T_x$-MXenes Components for Lithium-Sulfur Batteries: Suppressing the Shuttle Phenomenon through Physical and Chemical Adsorption. *ACS Nano* **2020,** *14* (8), 9744-9754.

38. Zhao, D.; Zhao, R.; Dong, S.; Miao, X.; Zhang, Z.; Wang, C.; Yin, L., Alkali-induced 3D crinkled porous Ti_3C_2 MXene architectures coupled with NiCoP bimetallic phosphide nanoparticles as anodes for high-performance sodium-ion batteries. *Energy Environ. Sci.* **2019,** *12* (8), 2422-2432.

39. Mahalingam, S.; Abdullah, H.; Manap, A., Role of acid-treated CNTs in chemical and electrochemical impedance study of dye-sensitised solar cell. *Electrochimica Acta* **2018,** *264*, 275-283.

40. Li, F.; Liu, Y.-L.; Wang, G.-G.; Zhang, H.-Y.; Zhang, B.; Li, G.-Z.; Wu, Z.-P.; Dang, L.-Y.; Han, J.-C., Few-layered $Ti_3C_2T_x$ MXenes coupled with Fe_2O_3 nanorod arrays grown on carbon cloth as anodes for flexible asymmetric supercapacitors. *Journal Of Materials Chemistry A* **2019,** *7* (39), 22631-22641.

41. Rao, D. W.; Zhang, L. Y.; Wang, Y. H.; Meng, Z. S.; Qian, X. Y.; Liu, J. H.; Shen, X. Q.; Qiao, G. J.; Lu, R. F., Mechanism on the Improved Performance of Lithium Sulfur Batteries with MXene-Based Additives. *J. Phys. Chem. C* **2017,** *121* (21), 11047-11054.

42. Li, G.; Lu, F.; Dou, X.; Wang, X.; Luo, D.; Sun, H.; Yu, A.; Chen, Z., Polysulfide Regulation by the Zwitterionic Barrier toward Durable Lithium-Sulfur Batteries. *J. Am. Chem. Soc.* **2020,** *142* (7), 3583-3592.

43. Liu, X.-F.; Chen, H.; Wang, R.; Zang, S.-Q.; Mak, T. C. W., Cationic Covalent-Organic Framework as Efficient Redox Motor for High-Performance Lithium-Sulfur Batteries. *Small* **2020,** *16* (34), 2002932.

44. Chen, W.; Lei, T.; Lv, W.; Hu, Y.; Yan, Y.; Jiao, Y.; He, W.; Li, Z.; Yan, C.; Xiong, J., Atomic Interlamellar Ion Path in High Sulfur Content Lithium-Montmorillonite Host Enables High-Rate and Stable Lithium-Sulfur Battery. *Adv. Mater.* **2018,** *30* (40), 1804084.

45. Zheng, S.; Wen, Y.; Zhu, Y.; Han, Z.; Wang, J.; Yang, J.; Wang, C., In Situ Sulfur Reduction and Intercalation of Graphite Oxides for Li-S Battery Cathodes. *Adv. Energy Mater.* **2014,** *4* (16), 1400482.

46. Meng, Z.; Li, S.; Ying, H.; Xu, X.; Zhu, X.; Han, W.-Q., From Silica Sphere to Hollow Carbon Nitride-Based Sphere: Rational Design of Sulfur Host with Both Chemisorption and Physical Confinement. *Advanced Materials Interfaces* **2017,** *4* (11), 1601195.

47. Wu, H.; Li, Y.; Ren, J.; Rao, D.; Zheng, Q.; Zhou, L.; Lin, D., CNT-assembled dodecahedra core@nickel hydroxide nanosheet shell enabled sulfur cathode for high-performance lithium-sulfur batteries. *Nano Energy* **2019,** *55*, 82-92.